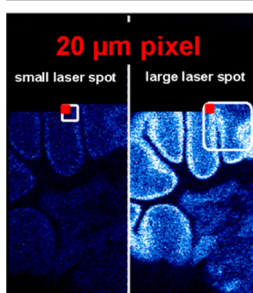


RESEARCH ARTICLE

Influence of the Laser Spot Size, Focal Beam Profile, and Tissue Type on the Lipid Signals Obtained by MALDI-MS Imaging in Oversampling Mode

Marcel Wiegelmann,¹ Klaus Dreisewerd,^{1,2} Jens Soltwisch¹ ¹Institute for Hygiene, University of Münster, Robert-Koch-Str. 41, 48149, Münster, Germany²Interdisciplinary Center for Clinical Research (IZKF), University of Münster, Domagkstr. 3, 48149, Münster, Germany

Abstract. To improve the lateral resolution in matrix-assisted laser desorption/ionization mass spectrometry imaging (MALDI-MSI) beyond the dimensions of the focal laser spot oversampling techniques are employed. However, few data are available on the effect of the laser spot size and its focal beam profile on the ion signals recorded in oversampling mode. To investigate these dependencies, we produced 2 times six spots with dimensions between ~30 and 200 μm . By optional use of a fundamental beam shaper, square flat-top and Gaussian beam profiles were compared. MALDI-MSI data were collected using a fixed pixel size of 20 μm and both pixel-by-pixel and continuous raster oversampling modes on a QSTAR mass spectrometer. Coronal mouse brain sections coated with 2,5-dihydroxybenzoic acid matrix were used as primary test systems. Sizably higher phospholipid ion signals were produced with laser spots exceeding a dimension of ~100 μm , although the same amount of material was essentially ablated from the 20 μm -wide oversampling pixel at all spot size settings. Only on white matter areas of the brain these effects were less apparent to absent. Scanning electron microscopy images showed that these findings can presumably be attributed to different matrix morphologies depending on tissue type. We propose that a transition in the material ejection mechanisms from a molecular desorption at large to ablation at smaller spot sizes and a concomitant reduction in ion yields may be responsible for the observed spot size effects. The combined results indicate a complex interplay between tissue type, matrix crystallization, and laser-derived desorption/ablation and finally analyte ionization.

matrix were used as primary test systems. Sizably higher phospholipid ion signals were produced with laser spots exceeding a dimension of ~100 μm , although the same amount of material was essentially ablated from the 20 μm -wide oversampling pixel at all spot size settings. Only on white matter areas of the brain these effects were less apparent to absent. Scanning electron microscopy images showed that these findings can presumably be attributed to different matrix morphologies depending on tissue type. We propose that a transition in the material ejection mechanisms from a molecular desorption at large to ablation at smaller spot sizes and a concomitant reduction in ion yields may be responsible for the observed spot size effects. The combined results indicate a complex interplay between tissue type, matrix crystallization, and laser-derived desorption/ablation and finally analyte ionization.

Keywords: MALDI-MSI, Continuous raster mode, Oversampling, Square flat-top beam profile, Fundamental beam shaper

Received: 1 July 2016/Revised: 3 August 2016/Accepted: 4 August 2016/Published Online: 22 August 2016

Introduction

Matrix-assisted laser desorption/ionization mass spectrometry imaging (MALDI-MSI) is an emerging technique for the analysis of biological surfaces, in particular microtome sections of animal and plant tissues [1, 2]. The technique enables simultaneous label-free visualization of the lateral distribution of numerous biomolecules in the sections (e.g., peptides, lipids, further metabolites). With current MALDI-MSI instruments, lateral resolutions in the range of a few 10 μm are

routinely achieved, and several reports even demonstrated MALDI-MSI analysis with pixel sizes in the low micrometer range [3–7].

Whereas the lateral resolution of a MALDI-MSI analysis is largely defined by the focal laser spot size, one possibility to improve it beyond this value is via oversampling. In this acquisition mode, the pixel size (i.e., the step size of the sample stage) is smaller than the employed laser spot. Each position on the sample is irradiated by multiple laser shots until the ion signal intensities have significantly dropped (ideally to zero); typically, this is achieved after full ablation of material within the irradiated zone, which necessitates either the use of a laser with high repetition rate or that of high laser fluences. After incremental translation of the sample stage, only freshly irradiated material contributes to the ion signals produced from this new pixel.

Electronic supplementary material The online version of this article (doi:10.1007/s13361-016-1477-y) contains supplementary material, which is available to authorized users.

Correspondence to: Jens Soltwisch; e-mail: jenssol@uni-muenster.de

Oversampling was introduced for MALDI-MSI by Jurchen et al. in 2005 [8]. Using a $100 \times 200 \mu\text{m}^2$ -wide laser spot in combination with a MALDI time-of-flight (TOF) mass spectrometer (Voyager DE-STR; AB SCIEX, Concord, ON, Canada) a lateral resolution of about $25 \mu\text{m}$ was demonstrated for the analysis of peptides prepared on electroformed nickel grids. MSI studies performed with tissue sections demonstrated an even higher gain in lateral resolution. For example, Garate et al. recently reported a lateral resolution of $\sim 5 \mu\text{m}$ for the MALDI-MSI analysis of lipids from colon sections using a hybrid LTQ-Orbitrap XL mass spectrometer (Thermo Fisher Scientific, Waltham, MA, USA), despite of the strongly elliptical laser spot ($37 \times 160 \mu\text{m}^2$) produced by the mounted laser system [9]. Using a hybrid MALDI Synapt G1 orthogonal-TOF mass spectrometer (Waters, Milford, MA, USA), Snel and Fuller achieved a resolution of about $15 \mu\text{m}$ for the MSI analysis of glucosylceramides from spleen tissue sections; in this case, the focal laser beam had a $1/e^2$ -diameter of $\sim 150 \mu\text{m}$ [10].

Next to lateral resolution and analytical sensitivity, data acquisition time is another particularly important factor for the applicability of the MALDI-MSI technology. One way to cut down this value is by use of the so-called continuous raster mode. In contrast to the more commonly used pixel-by-pixel approach, where a fixed number of laser pulses is applied per pixel to record a single mass spectrum, in continuous raster mode the MALDI sample stage is moved continuously. The advantage of this approach is that dead times (e.g., caused by time-consuming step motor control operations) are reduced. Most straightforwardly, the continuous raster mode is combined with hybrid mass spectrometers that enable continuous ion detection, similar as for electrospray ionization (ESI) MS. Single “pixels” are later-on retrieved from the continuous scan *in silico* by setting fixed time [11].

Using a QSTAR oTOF instrument, similar to the one employed in the present study, Trim et al. reported a 6-fold reduction in MALDI-MSI acquisition time. In their work, a 10 kHz-Nd:YVO₄ laser was used with a pixel size of $150 \mu\text{m}$ [12]. The manufacturer of the QSTAR spectrometer (AB Sciex) reported similar time-saving values in a technical note, with a possible lateral resolution in the raster-direction of about $30 \mu\text{m}$ using a laser spot size of $150 \mu\text{m}$ [13].

Although the MALDI technique was introduced already about three decades ago [14] and has evolved into an established method for the mass spectrometric analysis of many biomolecular classes (e.g., in the fields of proteomics and lipidomics [15, 16]), details of the complex desorption and ionization processes remain in part still unclear [17–20]. Numerous fundamental studies were conducted to investigate the influence of relevant “input parameters” on the MALDI ion yields, like the type and physicochemical properties of the MALDI matrix [21], the analyte-to-matrix ratio in the sample [22], or those of the laser irradiation parameters like wavelength [23–25], fluence [23, 24, 26–29], and pulse width [30, 31].

The effect of the laser spot size has been investigated roughly between 1.5 and $300 \mu\text{m}$ for both Gaussian [28, 32] and flat-top beam profiles [23, 24, 26, 27, 29]. These studies

generally revealed a strong increase of the ion detection threshold (and optimal fluence for maximizing the ion yields) with decreasing spot size that was larger than the reduction in irradiated area.

Next to ion intensities, also material ejection under MALDI conditions was investigated. Generally, two regimes are most widely considered to account for the release of intact gas-phase molecules from the condensed phase [17, 19, 33]. At lower laser fluences, thermal molecular desorption results predominantly in the formation of gas-phase monomers. Above a critical energy density, a change to an ablation regime leads to the ejection of a mixture of clusters and monomers. Molecular dynamics studies have shown that the transition point will depend strongly on the specific material and laser irradiation parameters (including, in particular, the laser fluence and pulse duration) [19, 34, 35].

Also, the beam intensity profile can presumably contribute to changes in the material ejection. For example, Holle et al. compared the MALDI ion yields as obtained with Gaussian beams and structured profiles containing “hot spots” [36]. They observed a significant gain in peptide ion yield desorbed from different matrices upon using the structured beam.

To simplify experimental conditions and to single out one of the many parameters involved, most fundamental experiments have been performed with one of the classic MALDI matrices [e.g., 2,5-dihydroxybenzoic acid (DHB) or α -cyano-4-hydroxycinnamic acid (HCCA)], standard sample preparations protocols (e.g., the dried-droplet protocol where analyte and matrix are co-crystallized from solution directly on the sample stage), and easy-to-ionize test biomolecules (in particular basic peptides). However, MALDI-MSI experiments of real biological samples like tissue sections are distinctly more complex as was, e.g., shown by Römpf and Spengler in an overview article [37]. To address this additional complexity further, researchers have recently designed fundamental experiments in which matrix-coated tissue sections were used as “real-life” test systems. For example, Steven et al. performed experiments with mouse brain sections and investigated the phospholipid ion signals in dependence of beam profile, laser spot size, and laser fluence [29]. Notably, a fiber-based setup was used in this work that enabled production of square spot sizes. The possible advantage of this irradiation geometry for oversampling MALDI-MSI has previously been discussed [38].

Even with all these fundamental works taken into consideration, many MALDI-MSI analyses are nevertheless still “you see what you ionize” experiments. Contrast-rich images of well-ionizing molecules (e.g., phosphatidylcholines, PC) are produced without ultimately knowing if real biological differences (abundances of the molecules in the tissue areas) are correctly reflected by the MSI data. In particular, ion suppression effects can readily alter the ion images [39, 40]. Also, an altered degree of analyte extraction from different parts of the tissue section during sample preparation may influence the detected analyte distribution. Owing to these complications, MALDI-MS imaging data are generally challenging to interpret, in particular with respect to quantitation; often a validation

with another technique, e.g. histologic information [41] is unavoidable. However, several promising approaches have been introduced to overcome these problems and to enable quantitative imaging of targeted substances. In particular, the use of well-chosen internal standards has been shown to offer a powerful means for improving quantification in (Q)MALDI-MSI. A timely review of different introduced approaches and addressing in particular QMALDI-MSI of lipids has recently been provided by Ellis et al. [42].

Here, we conducted a set of fundamental studies with the aim to obtain a better understanding about the role of the focal laser spot size and its beam profile in MALDI-MSI. To obtain particular defined excitation conditions we introduce a fundamental beam shaper (FBS) that enables the straightforward generation of square flat-top profiles. Gaussian beam profiles were used for comparison. By use of a telescope and generation of different numerical apertures at the final focusing lens, focal spot sizes were varied in the range from 30 to 200 μm . As a well-documented biological test system, we used coronal sections of murine brain (plus rodent kidney and testes in two additional experiments). DHB matrix was applied with a sublimation/recrystallization protocol. Control experiments were, moreover, performed with HCCA matrix and by spray-coating tissue sections with DHB. MALDI-MSI data were obtained in pixel-by-pixel and continuous raster oversampling scan modes.

Experimental

Chemicals

2,5-Dihydroxybenzoic acid, α -cyano-4-hydroxycinnamic acid, and 2-hydroxyethylcellulose (average molecular weight, MW_{av} , 1,500,000) were from Sigma-Aldrich (Steinheim, Germany) and used as supplied. Organic solvents were from different suppliers and were of $\geq 99\%$ purity. Water was purified with a Synergy system (Merck Millipore, Darmstadt, Germany).

Preparation of Tissue Sections

Murine brains and kidneys were dissected from 13- to 14-wk old female C57BL/6 mice. Testes were from white Lewis rats (LEW/Crl; Charles River Laboratories, Sulzfeld, Germany). Immediately after dissection, organs were snap-frozen in liquid nitrogen and stored at $-75\text{ }^{\circ}\text{C}$ until further use. All animal material was acquired according to standard protocols and approval by the local ethics commission. To facilitate sectioning, organs were embedded in 2-hydroxyethyl cellulose polymer; 16 μm -thick tissue sections were produced with a cryomicrotome (Jung Frigocut 2800-E; Leica, Wetzlar, Germany) at $-20\text{ }^{\circ}\text{C}$ and thaw-mounted onto standard (non-coated) histologic glass slides. All mouse brain sections used were from a region between 11 and 12 mm from bregma, with a slightly oblique cut.

Preparation of Tissue Sections from Homogenized Porcine Brain

A whole porcine brain was obtained from a local butchery. The organ was frozen to $-75\text{ }^{\circ}\text{C}$, cut into small pieces with a scalpel, rapidly minced in a blender, and further homogenized for 5 min using a manual disperser (Polytron PT1200; Kinematica, Lucerne, Switzerland); 10–13 mL of the frozen slush were filled into a slightly conical centrifugation tube (15 mL Falcon tube with $\sim 9\text{ mm}$ inner diameter). Tubes were lightly centrifuged for about 60 s to remove air bubbles and flash-frozen in liquid nitrogen. The cylindrical core was removed from the tube by light tapping on the back end and cut into $\sim 20\text{-mm}$ -long sections using a scalpel. Single pieces were freeze-mounted onto a cryotome holder using a drop of water. Sixteen μm -thick sections were prepared and thaw-mounted as described above.

Coating of Tissue Sections with MALDI Matrix

Two different matrix coating protocols were used. The sublimation/recrystallization approach was adopted from [43]. This protocol was applied in all MS imaging experiments except for one control experiment. Briefly, the histologic glass slides with sections mounted were first cut to smaller, approximately $26\text{ mm} \times 26\text{ mm}$ wide pieces. Single slides were fixed inside a vacuum chamber (maintained at a pressure of ca. 5×10^{-5} mbar) to a water-cooled glass cylinder, mounted approximately 8 cm above a matrix reservoir containing $\sim 175\text{ mg}$ of matrix powder. DHB matrix was sublimated at $125\text{ }^{\circ}\text{C}$ for 8 min, HCCA at $170\text{ }^{\circ}\text{C}$ for 30 min. After withdrawal from the vacuum chamber, sections were allowed to recrystallize at $75\text{ }^{\circ}\text{C}$ for 2.5 min (DHB) or 4 min (HCCA) in a saturated atmosphere of H_2O :methanol (1000:5 v/v). Using this protocol, homogenous microcrystalline matrix preparations were obtained for both matrices. Using Secondary Electron Microscopy (SEM), mean crystal sizes were determined to $\leq 10\text{ }\mu\text{m}$.

The second protocol was adopted from [44] and based on spray-coating the tissue sections with a semi-automated artistic airbrush sprayer, equipped with a $150\text{-}\mu\text{m}$ nozzle (Infinity Solo; Harder and Steenbeck, Norderstedt, Germany). In this case, DHB was dissolved to 50 mg/mL in methanol/water 2:1 (v/v). The distance of the airbrush outlet to the sample was set to 20 cm. Ten spraying cycles of 5 s duration were followed by intermittent 20 s long drying intervals. The N_2 back pressure of the airbrush system was adjusted to 3.5 bar and the gas flow maintained during the drying phase to force solvent evaporation.

Hematoxylin and Eosin (H&E) Staining

H&E stains were obtained after the MSI runs by washing the matrix from the sections with chloroform/methanol (2:1, v/v). Damage to the tissue section due to the laser irradiation was not visible for any of the used experimental conditions. Presumably, the investigated tissues can be assumed to be essentially opaque at the Nd:YAG laser wavelength of 355 nm.

Mass Spectrometry

Mass spectra were recorded with an orthogonal-extracting time-of-flight (oTOF) mass spectrometer (QSTAR pulsar-i; AB SCIEX, Concord, ON, Canada). The mass resolution was ~ 5000 (FWHM) at m/z 800 and the mass accuracy ~ 15 ppm using internal calibration with known lipid species (the abundant phospholipid $[\text{PC}(34:1) + \text{K}]^+$, detected at m/z 798.54, its fragment with a loss of $\text{N}(\text{CH}_3)_3$ found at m/z 739.47 as well as $[\text{PC}(40:1) + \text{Na}]^+$ at m/z 866.66 were used). These three prominent ions (known to be present in high concentration in mouse brain [7]) were covering the primarily investigated lipid range of m/z 650 to 1000 well (Supplementary Table S2). The oMALDI2 ion source (AB SCIEX) of the instrument was modified as described previously for an identical instrument [45, 46] to enable adjustment of buffer gas pressures in the ion source; 0.7 mbar of N_2 were used throughout all MS experiments. A second modification concerned swapping the default laser and CCD camera observation ports. Moreover, the default fiber-based laser beam delivery system was omitted, such that the laser beam was coupled into the MALDI source as a free beam. Use of the “side port” of the oMALDI2 ion source instead of the default port, which is located on top of the ion source, had the advantage that all laser beam alignment was achieved in a single horizontal plane. To increase the reflectivity, the mirror mounted in the default camera beam path—now used for laser beam delivery—was replaced with a laser grade aluminum surface mirror.

Laser Beam Shaping/Steering and Online-Control of Focal Beam Profiles

The overall setup for beam shaping, steering, and online-control of focal intensity profiles is outlined in Figure 1a. A Nd:YAG laser (wavelength, 355 nm; pulse width, 10 ns; maximum pulse repetition rate, 300 Hz; pulse energy, 120 μJ ; Diodescope; Bioptic Lasersysteme, Berlin, Germany) was used in all experiments. This laser produces a near TEM_{00} profile with a high beam quality factor M^2 of ~ 1.15 . The pulse energy of the laser was fine-adjusted using two dielectrically-coated attenuators for 355 nm (Laseroptik, Garbsen, Germany). The attenuators were rotated in opposite direction to each other to exploit the angle-dependent transmission characteristics and to simultaneously compensate for beam displacements. A fundamental beam shaper (FBS2; TOPAG, Darmstadt, Germany) was mounted 75 cm behind the laser exit aperture; at this position the laser beam was 2 mm wide. The properties of the FBS and requirements for its implementation are discussed in the Results and Discussion section. Optional beam size expansion or reduction was achieved with a telescope consisting of pairs of fused silica lenses with different focal lengths. The diameter of all lenses was 25 mm. A fused silica lens with a focal length of 250 mm served for focusing the expanded beam onto the MALDI target at an angle of incidence of $\sim 45^\circ$.

Using a fused silica beam splitter (model 30R/70 T; Edmund Optics, Barrington, NJ, USA) mounted at 45° , $\sim 30\%$ of the overall light intensity was redirected onto the CCD chip of a

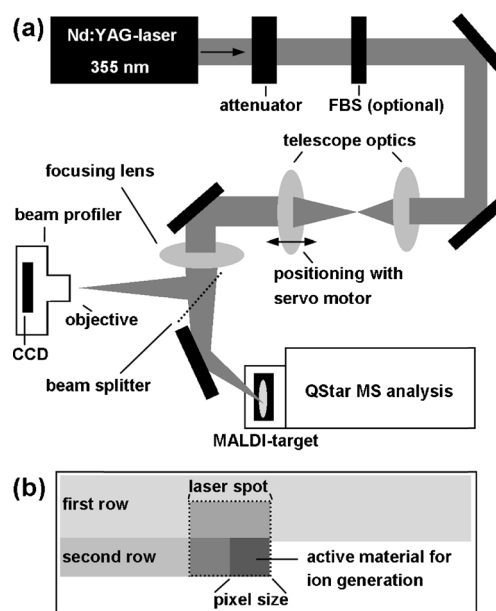


Figure 1. (a) Set-up for laser beam shaping, steering, and online-control of focal beam intensity profiles and pulse energies. (b) Scheme illustrating the continuous-raster oversampling mode

beam profiler (SP620; Ophir Spiricon, Darmstadt, Germany) that was equipped with a $13.6\times$ magnifying objective. The pixel to pixel distance of the CCD chip of the beam profiler is $4.4\ \mu\text{m}$, leading to an effective resolution of $0.32\ \mu\text{m}$ with the employed optics. Great care was taken that this element was placed at exactly the same distance from the beam splitter and focusing lens as the MALDI sample plate. This fine-adjustment was achieved by monitoring beam profiles and the laser-induced ablation craters formed on thin microcrystalline preparations of DHB matrix on the MALDI target.

Diameters for the Gaussian beam profile and the edge length for the flat-top beam profiles, respectively, were calculated using the 4σ definition [47]. To calculate absolute fluence values (laser pulse energy per irradiated area), signal intensities as obtained with the beam profiler were furthermore calibrated with a pyroelectric energy meter (PEM100; LTB Lasertechnik, Berlin, Germany).

MALDI-MS Imaging

All MS experiments were performed in positive ion mode using oMALDI server (version 5.1, AB SCIEX) and Analyst software (version 1.1, AB SCIEX). The transmission range of the quadrupole transfer system of the hybrid mass analyzer was set to m/z 650–1000. In this way, abundant phospholipids were detected with highest sensitivity and, at the same time, file sizes generated during the extended MSI experiments, some of which were encompassing the analysis of whole mouse brain sections, could be kept at an acceptable level. Image acquisition was done in classic pixel-by-pixel mode or in continuous raster mode. In both scan modes, the MSI pixel size was kept constant at $20\ \mu\text{m} \times 20\ \mu\text{m}$. Because the cross-section of the focal

laser beams exceeded the 20 μm -pixel size for all realized spots, varying degrees of oversampling occurred.

In the pixel-by-pixel mode, single mass spectra were acquired by applying 100 laser shots. In the continuous raster mode, the sample stage was moved continuously along one horizontal line at a speed of 0.2 mm/s (the lowest adjustable via the control software), before the stage was moved back to start the next parallel line, 20 μm beneath the first. Single pixel mass spectra were in this case generated *in silico* by scanning over 0.1 s. With a laser repetition rate of 300 Hz, this corresponds to 30 applied laser pulses and translation of the sample stage over a distance of 20 μm ; per single laser pulse the stage thus moved by about 600 nm. The principle of the continuous raster mode is illustrated in Figure 1b.

Imaging Data Processing

The imaging data files were converted with the oMALDI Server 5.1 software to “analyze format” using a bin width of 0.1 Da and were subsequently loaded into BioMap software (version 3.8.0.4; Novartis, Switzerland) for further processing. This program also provides a means for drawing a region of interest (based on the MSI data) and to extract sum mass spectra from these areas.

To obtain intensity line scans of the MS data, the false color ion images as produced with BioMap were exported to tiff format and then loaded into ImageJ (ImageJ 1.48 k; National Institutes of Health, Bethesda, MD, USA) for further evaluation. Further data processing was done using OriginPro 2015 software (OriginLab Corporation, Northampton, MA, USA).

Lipid Assignments

Tentative lipid assignments were based on comparing calculated masses, taken from Lipid Maps data base (<http://lipidmaps.org>) to experimental values and using a 15 ppm accuracy criterion. To compensate for the relatively low resolving power of 5000 of the second generation QSTAR pulsar I, tentative assignments were made only if the proposed lipid species were described previously in the literature [5, 7, 48, 49] to be present in mouse brain. This does not rule out that in some cases further (low-abundant) lipid ion species may have contributed to the ion signal. Full structural characterization of the compounds was beyond the scope of the present paper but has, for mouse brain, been provided before (see, e.g., the references above).

Safety Hazard Note

The employed laser is of safety class 4. Suitable safety measures, (e.g., wearing protective goggles and assigning laser laboratory space) have to be established upon working with free beams of such lasers.

Results and Discussion

Generation of a Flat-top Beam Using a Fundamental Beam Shaper

Inserting the FBS into the laser beam path (Figure 1a) provided an easy to establish yet powerful means for producing square flat-top intensity profiles on the MALDI target. Compared with the frequently used fiber-based approaches [23, 24, 27, 29], the FBS is uncritical concerning the laser fluence (i.e., damage thresholds) under MALDI-typical conditions and also concerning speckle effects. However, a main prerequisite for obtaining the desired beam patterns with this modulating element is the use of a laser with high beam quality ($M^2 \leq 1.2$). Secondly, the FBS is manufactured for a specific laser beam illumination diameter, in our case 2 mm. With these conditions met, changing the beam profile from Gaussian to flat-top was a simple flip of the FBS in or out of the beam path.

In the present study, six different focal spot sizes with widths between 30 and 130 μm for the Gaussian and 50–200 μm for the flat-top beam, respectively, were realized by using different lens combinations in the telescope mounted behind the FBS (Figure 1a), thereby adjusting the numerical aperture for the final focusing. The difference of $\sim 1.5\times$ in the beam widths/diameters between the flat-top and Gaussian profiles is due to the working principle of the FBS modulator.

Two representative flat-top and Gaussian intensity profiles recorded with a high resolving beam profiler, mounted at the same distance from the focusing lens than the MALDI target (Figure 1a), are plotted in Figure 2a, c; the well-defined Gaussian profile of the unaltered beam (2c) is effectively transformed into a square flat-top profile exhibiting sharp flanks and a homogenous plateau region (2a). Next to the central plateau, the FBS also generated side lobes with a maximum intensity of $\sim 5\%$ – 10% of the central region. These are, for instance, visible in line scans through the profiles, plotted at the left and bottom side of the 2D-profiles in Figure 2a, c. Owing to the low energy content in these lobes, they did, however, in no case generate visible material ablation, unless excessively high, MALDI-untypical laser fluences were applied. Ablation craters as generated at MALDI-typical fluence conditions with the two flat-top and Gaussian profiles are plotted in Figure 2b, d.

Attributable to the angle of incidence of the laser beam onto the sample stage of 45° , the spots on the MALDI target are about 1.44-fold wider in this direction than those imaged by the high resolving beam profiler. All obtained spot dimensions are summarized in Supplementary Table S1 for the actual MALDI conditions. Due to the limited depth of field (DoF), accurate fine-focusing of the beam onto the MALDI target (and beam profiler) was necessary, especially for small laser spots. This was achieved by servo-controlled positioning of the second telescope lens (Figure 1a) in increments of 20 μm and observing the obtained profiles with the beam profiler. For example, for the smallest realized spot of $33 \mu\text{m} \times 26 \mu\text{m}$ with a Gaussian beam profile, the position of the second telescope lens had to be adjusted to an accuracy of about $\pm 200 \mu\text{m}$. Owing to its working principle, the position of the second telescope lens

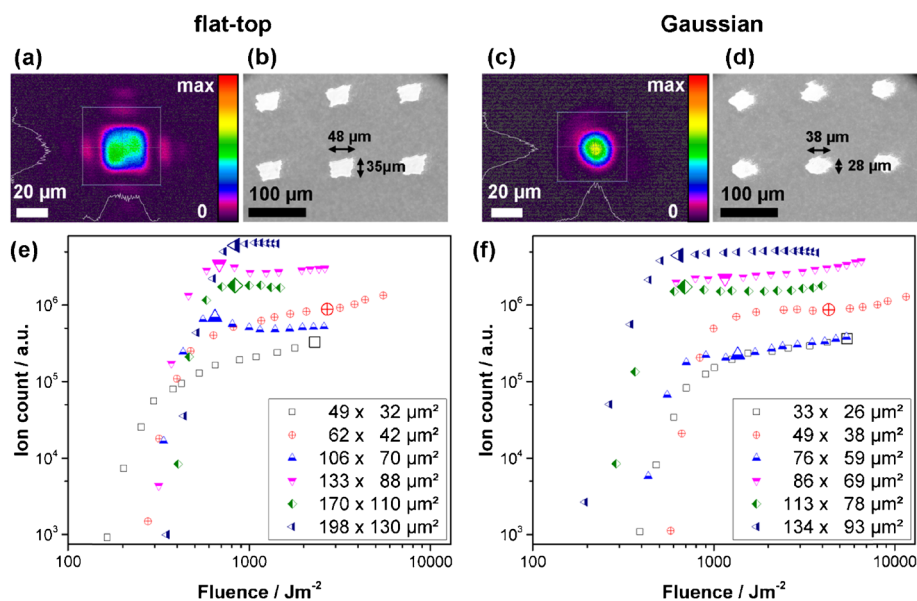


Figure 2. (a), (c) Intensity profiles of the smallest flat-top ($49 \times 32 \mu\text{m}^2$ on target) and Gaussian beams ($33 \times 26 \mu\text{m}^2$), respectively, as measured with the beam profiler. Intensity line scans through the central axes of the spots are depicted on the left and bottom side. (b), (d) Optical images of the ablation craters produced in a thin DHB matrix layer with the two beams. (e), (f) Total ion counts in the m/z region 650 to 1000 (phospholipid mass range), in dependence of the focal laser spot size and applied laser fluence for the flat-top and Gaussian beam profiles. Data were obtained by irradiating single 3-mm-long lines across homogenized porcine brain tissue, each using the continuous raster mode. Fluences producing optimal MS imaging contrasts for each spot size are indicated by an enlarged symbol; absolute fluence values are listed in Supplementary Table S1 of the Electronic Supplementary Material

was more critical using the FBS. The square flat-top profile for the smallest realized spot of $49 \times 32 \mu\text{m}$ was only met with a position accuracy of the second telescope lens of about $\pm 40 \mu\text{m}$.

Ion Signal Intensities as a Function of Laser Fluence and Spot Size

To characterize the influences of the focal spot size and laser fluence on the generation of the phospholipid ions in MALDI-MSI, as well as to determine optimal laser fluences for the imaging experiments performed in continuous raster mode, we conducted a set of fundamental experiments. Homogenized porcine brain sections were used to simulate true MALDI-MSI conditions, while at the same time ensuring a homogeneous signal response. Fluences ranging from the ion detection thresholds to up to 15 times these values were applied. For each spot size setting, a set of fresh raster-lines (3 mm long) was irradiated with the different laser fluences in continuous raster mode, with a total of 4500 laser pulses for each line.

Total ion counts (TIC) that were obtained as a function of fluence and spot size in the m/z range from 650 to 1000 (comprising all major phospholipids except cardiolipins) are plotted in Figure 2e for excitation with the flat-top and in Figure 2f for excitation with the Gaussian profiles. The data reflect the well-known sharp threshold behavior of ion generation in MALDI and the exponential signal increase [23, 24, 26–28]. After the initial increase, approximately at values three to four times the threshold fluence, however, spot size-

dependent effects set in. While for spot sizes with dimensions below approximately $75 \mu\text{m}$, the TICs showed a further increase, albeit with a reduced slope, for larger spots above $75 \mu\text{m}$ in width/diameter, the TICs essentially reached a saturation plateau. For the larger spot sizes, these findings are in line with MALDI results obtained previously with dried-droplet sample preparations [23, 27, 28]. Essentially, they also reproduce the recent results obtained by Steven et al. [29] with both coated tissue sections and thin-layer sample preparations. The smallest dimensions produced in that work were about $50 \times 120 \mu\text{m}^2$ and might just have been above the transition point toward a different signal intensity-fluence behavior. Moreover, a different MALDI matrix (HCCA) was used as well as a more structured focal beam profile containing an array of hot spots (speckles).

The mass spectra acquired at the different spot sizes/fluence settings were also analyzed regarding possible fragmentation processes and/or production of matrix clusters as both effects could possibly distort the mass spectra. Significant abundances of DHB matrix clusters were not detected from matrix-coated tissue areas in the m/z range from 650 to 1000 at all laser fluences and spot sizes. Low-abundant matrix clusters were only detected if matrix-coated glass slides away from the tissue sections were investigated. Upon irradiation of matrix-coated tissue, they are either not produced or quantitatively reduced by ion suppression. Therefore, we tentatively assume that at least 90% of the ion counts in the investigated m/z region were produced by tissue-derived compounds. As expected, fragmentation processes increased to some extent with increasing

fluence. As an example, Supplementary Figure S1 depicts the prominent loss of $N(\text{CH}_3)_3$ from the most abundant PC(34:1) ion species in relation to the sum of the intact ion and the fragment ion at a large and a small spot sizes. Significantly less fragmentation of PC was observed in the high fluence range when the smaller spot was used. For the large spot, the intact PC ion signals decreased for fluences above the optimized fluence. This is in line with the overall different behavior of the TIC for smaller and larger spot sizes as seen in Figure 2e, f, and discussed above.

We used the produced extensive data set to identify compromises between an optimized TIC and acceptable dissociation rates for the following MALDI-MSI imaging study. As a consequence of the combined spot size/laser fluence effects, different optimized fluences were selected for different spot sizes. Their values are annotated in Figure 2e, f, by enlarged symbols and listed in Supplementary Table S1. These optimized fluences are slightly elevated compared with typical values employed in MALDI experiments at comparable spot sizes [17].

Comparison of Pixel and Continuous-Raster Imaging

Compared with the pixel-to-pixel mode, the continuous raster mode was nearly 10 times faster and, therefore, a similar improvement as the 6-fold gain reported by Trim et al. [12] was achieved. In this way, a whole coronal mouse brain section (about 6 mm \times 9 mm wide) could be imaged using a pixel size of 20 μm within 4.5 h. Interestingly, despite of the lower number of 30 versus 100 laser pulses applied, the signal-to-noise (S/N) ratios of the ion images were generally higher in rastering mode. Most likely this effect can be explained by different ion detection procedures of the instrument in the two used modes rather than changes in ion generation. Unlike in axial TOF-instruments, ion generation and mass spectrometric measurement are energetically decoupled in orthogonal setups like the QSTAR. This spreads the arrival times of ions at the analyzer to a more or less constant stream of ions beyond the time of laser fire. While in the pixel-per-pixel imaging method the QSTAR-instrument starts and stops the data acquisition for each pixel (inducing possible dead times in order to save a spectrum for each separate pixel), in the continuous-raster method each line is recorded as a whole and single pixels are derived later from set time frames.

A comparison of the two (raster and pixel-by-pixel) scan modes is shown in Figure 3b at the example of $[\text{PC}(36:4) + \text{K}]^+$ (m/z 820.52) recorded from four coronal brain sections. The characteristic, readily discernible morphologic fine features, as produced by myelin-rich white matter (WM) areas and surrounding gray matter (GM) areas in cerebellum, change only little over the overall cut depth of about 180 μm for 12 sections. The MS images showed that this is also the case for the lipid composition of specific areas. Therefore, this set of adjacent brain sections was selected as a “real-life” sample system for characterizing the effects of laser irradiation conditions on the outcome of MALDI-MSI measurements.

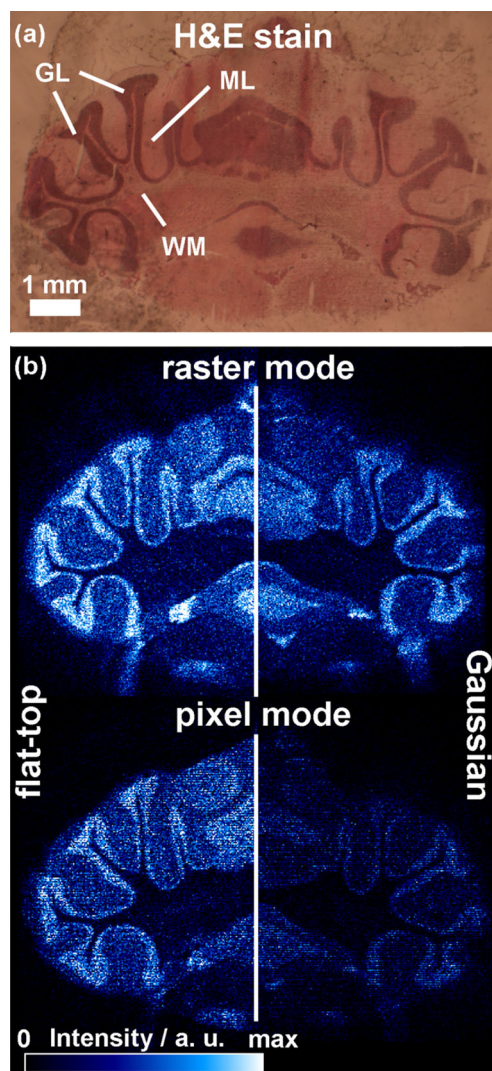


Figure 3. (a) H&E stain of a coronal mouse brain section, indicating areas of white (WM) and gray matter (GM), the latter consisting of granular layer (GL) and molecular layer (ML). (b) MALDI-MSI experiments visualizing the distribution of PC(36:4) ($[\text{M} + \text{K}]^+$ ion at m/z 820.52) in adjacent mouse brain sections. The top MS images were obtained in continuous raster mode, the bottom ones from consecutive sections in pixel-by-pixel mode. The left hemispheres of the brain sections were scanned with a flat-top beam (spot size: 133 \times 88 μm^2), the right hemispheres with a Gaussian beam (134 \times 93 μm^2); the white line was inserted in the optical image to differentiate the two hemispheres. The H&E stain in (a) was obtained from the section used for raster mode imaging with the flat-top beam after removing the matrix layer by washing of the section

Exploiting the mirror symmetry of the two brain hemispheres, the MALDI-MSI imaging properties of the two excitation profiles could be directly compared. In this experiment, the left hemispheres were measured with the FBS-generated flat-top beam (spot size: 133 \times 88 μm^2) and the right hemispheres with the Gaussian profile (spot size: 134 \times 93 μm^2). Comparing the MS data with an H&E stain of the section

(Figure 3a, middle) demonstrates that major brain areas (e.g., WM and GM) were well differentiated in all four modes. Image quality in the pixel-by-pixel mode, however, suffered from horizontal striping, an artefact that is caused by an inaccurate stage movement of the oMALDI2 source. This drawback, inherent to the employed sample stage, was not found in the continuous raster mode.

As could be expected already from the data presented in Figure 2e, f, similar signal-to-noise (S/N) ratios were obtained with flat-top and Gaussian beams (Figure 3b). Notably, a more pronounced S/N difference was apparent if flat-top and Gaussian beams were compared in the pixel-by-pixel mode (Figure 3b, bottom). Further experiments will be needed to investigate possible mechanistic differences.

Evaluation of the Lateral Resolution

All following experiments were performed with flat-top beams and using the continuous raster mode. At optimized laser fluences (see above) the TIC dropped significantly only after up to 50 laser shots on irradiated areas depending on the employed laser fluences. With this value exceeding the 30 shots per pixel applied during the MSI runs, the lateral resolution in the (horizontal) raster-direction must be assumed to suffer from incomplete material removal during the acquisition of one pixel. With a fixed pixel size of $20\ \mu\text{m} \times 20\ \mu\text{m}$, in some cases ion signal may not be attributed to the correct pixel, but found in the spectra assigned to the overlapping one. After complete irradiation of all pixels, however, nearly all matrix material was removed from the imaged area for all spot sizes. In the future, the described shortcomings could be overcome by the use of a higher pulse repetition rate laser or a slower translation of the stage.

To evaluate the loss of lateral resolution for different spot sizes, we compared ion images that were acquired by scanning the laser beam over a well-defined morphologic structure of the WM in cerebellum. The H&E stain of the analyzed region (Figure 4a, middle) revealed a width of the investigated structure of about $50\ \mu\text{m}$. MS images of $[\text{PC}(\text{O}-38:2) + \text{K}]^+$ (m/z 838.62), a plasmalogen that was only found in the WM, are shown in Figure 4a (left and right). The depicted ion images were recorded with spot sizes of $49 \times 32\ \mu\text{m}^2$ and $133 \times 88\ \mu\text{m}^2$, respectively. To reduce statistical errors (Figure 4c), five parallel lines just next to each other were examined for each spot size. As illustrated in Figure 4b, Gaussian functions were fit to the obtained data points and the full widths at half maximum (FWHM) used as a rough measure for the MS-derived widths of the structure. The derived values suggest that the $50\ \mu\text{m}$ width of the WM structure was accurately reproduced to $45 (\pm 8)\ \mu\text{m}$ (2.5 pixels) with the smallest laser spot size of $49 \times 32\ \mu\text{m}^2$. Using larger spots, the structure was not reflected correctly (i.e., the width was slightly overestimated). Interestingly, the observed loss in lateral resolution by a factor of up to two remained relatively constant even for the largest laser spot size of $200\ \mu\text{m}$ in width.

Data for the (vertical) non-raster direction are summarized in Supplementary Figure S2. In these experiments, a WM

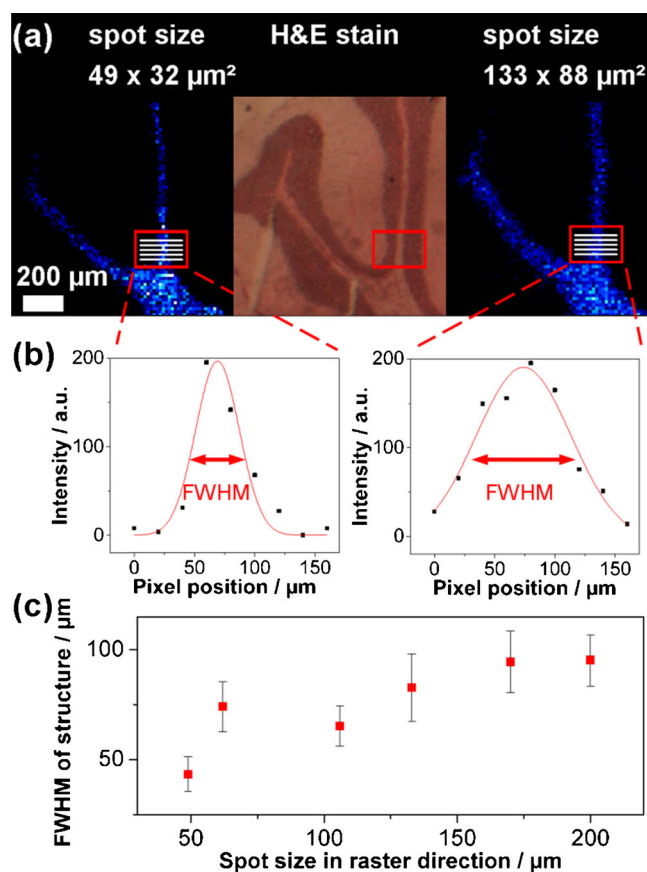


Figure 4. (a) Ion images of $[\text{PC}(\text{O}-38:2) + \text{K}]^+$ (m/z 838.62) recorded from coronal mouse brain sections with (left) $49 \times 32\ \mu\text{m}^2$ and (right) $133 \times 88\ \mu\text{m}^2$ flat-top beams in continuous raster mode. The H&E image (middle) was obtained from the section to the right after washing the matrix. (b) Intensity of the $[\text{PC}(\text{O}-38:2) + \text{K}]^+$ signal as a function of pixel position. Horizontal lines across the areas indicated in (a) by red boxes were evaluated. The pixel intensity data were fitted with Gaussian functions to derive FWHM values as a measure for the apparent MSI-derived width of the WM structure; the H&E stain in (a) revealed its width to $50\ \mu\text{m}$. (c) FWHM values obtained in this way for all six realized laser spot sizes; mean values and error bars were derived by evaluation of five parallel horizontal lines as indicated in (a)

structure, which was optically determined to be $80\ \mu\text{m}$ wide, was imaged correctly for all spot sizes with widths below $110\ \mu\text{m}$ and only a minor broadening of a factor of ~ 1.3 was observed for larger spots.

It should be mentioned that the determination of lateral resolution in MALDI-MSI is far from straightforward [50]. Especially the choices of the examined spatial feature as well as the chosen m/z -value play key roles. Moreover, care has to be taken that all of the structure broadening is caused by the pixel overlapping and not also originating from an overall increase in intensity and sensitivity with larger spot sizes. Furthermore, imperfect alignment of consecutive tissue sections in the x- or y-direction may introduce another source of error to the measurement. While the accuracy of our data

should, therefore, not be overestimated, a certain loss of spatial resolution with larger laser spot sizes was clearly observed.

Comparison of MS Ion Images Obtained with Different Spot Sizes

Six different laser spot sizes with areas ranging from 1585 to 25740 μm^2 (Supplementary Table S1) were used to produce MS images from consecutive brain sections. Figure 5a, b show intensity maps of two ion species [PC(O-38:2) and PC(38:6)] that are each representative for the lateral distribution in mouse brain for a whole set of lipids (i.e., two groups). A list of tentatively identified lipids and the brain structures in which they are predominantly detected is provided in Supplementary Table S2. Figure 5a shows the distribution of [PC(O-38:2) + K]⁺ detected at m/z 838.62. Comparison with the H&E stain of one of the measured sections (Figure 3a) revealed that this plasmalogen (along with further lipid species) was solely found in the white matter (WM) of the mouse cerebellum, in line with previous findings [7]. For ion generation from the WM, no spot size effect on lipid signal intensity was observed (i.e., within the expected margin of error, the signal intensities were essentially constant for all spot sizes).

In Figure 5b the ion images of [PC(38:6) + K]⁺, detected at m/z 844.52, are displayed. This lipid is not found in the mass spectra of the WM but throughout the other brain regions, in particular the GM, including granular (GL) and molecular layer (ML), with varying signal intensities. Again, a whole group of lipids showed the same distribution across the brain sections (Supplementary Table S2). In contrast to the findings made on WM, the signal intensities of lipid ion species recorded from the GM showed a strong dependence on laser spot size. Almost no ion signals were produced with the smallest spot size of $49 \times 32 \mu\text{m}^2$. However, with increasing laser spot size, increasingly contrast-rich MS images were produced and concomitantly the S/N ratio of the ion signals in the mass spectra increased sizably. The abundances of the lipid ions recorded with the six different spot sizes are denoted in Supplementary Table S2.

To investigate these interesting findings further, we next analyzed the TICs that were obtained from WM and GM brain areas as well as the whole investigated tissue sections. Regions of interest (ROI) covering WM and GM across the whole sections were drawn as described in the Experimental section. Figure 5c shows the TICs for the six employed spot sizes. Two example mass spectra obtained from the different regions are displayed in Figure 5d. For smaller laser spot sizes below ca. 100 μm (edge length in raster-direction) sizably more ions were detected from the WM (black squares) than from the GM (red circles). With spot sizes above 100 μm (and the accompanied decrease in fluence in order to obtain optimal MSI data; Supplementary Table S1), the TICs converge. Visual inspection and a second MALDI-MS measurements of the tissue sections after the initial MALDI-MSI experiment revealed that after completion of the imaging run, most of the matrix material was ablated at all spot sizes (with stronger ablation with smaller spot sizes due to the higher fluences used). This rules out that

the observed spot size effect was merely caused by non-ablated matrix and analyte material at the smaller spot sizes.

From the tentative assignments of the observed lipid species no correlation with phospholipid type was apparent. The most obvious cause for the observed differences is, thus, the type of brain region from which the lipids were generated. Affirming these observations, Steven et al. recorded different ion detection threshold fluences on different regions of coronal mouse brain sections for lipids species present in WM and GM [29]. Altogether, this indicates the existence of MALDI-relevant parameters specific to the investigated type of tissue.

Further Tissue Types, Spray Sample Preparation Protocol, and HCCA Matrix

To test if the observed effects were independent of matrix application technique, type of MALDI matrix, and tissue type, we conducted a few additional experiments in which we included a spraying protocol for the preparation of DHB, the use of HCCA as a second common MALDI matrix (prepared by the sublimation/recrystallization protocol), and the use of murine kidney and rat testis tissues. In these experiments, we compared a small ($40 \times 28 \mu\text{m}^2$ -wide) and a larger ($105 \times 70 \mu\text{m}^2$) spot size. For mouse kidney and rat testis, the spot size effect was even more enhanced than for the brain sections (Figure 5e, f). Using the small spot size, only few low-contrast ion images for the most abundant lipid species could be recorded. With the larger laser spot, the ion counts increased by about an order of magnitude, leading to contrast-rich ion images of several lipid species. Under these irradiation conditions, structures of the renal cortex (Figure 5e, left) and the seminiferous tubules in testis (Figure 5f, left) were imaged with high contrast visualizing the signal intensity of different phospholipids ([PC(32:0) + K]⁺ for the renal section and [PC(38:5) + K]⁺ for the rat testis).

The MSI results obtained from mouse brain with the sprayed DHB matrix are shown and described in more detail in Supplementary Figure S3, and those obtained with the HCCA matrix in Supplementary Figure S4. In short, all findings concerning the spot size effects on murine brain were more or less reproduced with both of these test systems.

To investigate the influence of salt content on the spot size effect, a brain tissue section was washed with ammonium acetate according to Wang et al. prior to matrix coating to remove alkali salts [48]. Washing led to the expected shift towards protonated lipid species but also a sizable loss of signal intensity from WM. Here, a sizable number of lipid species detected as alkali adducts on unwashed tissue are not detected in their protonated form after washing.

Contrary to the unwashed tissue, the remaining protonated lipid signals, however, show a comparable spot size effects on WM and GM. We tentatively conclude that high signal intensity with small spot sizes, a unique feature to unwashed WM among all investigated tissues, is facilitated by high salt content, making it an important parameter for the observed phenomena.

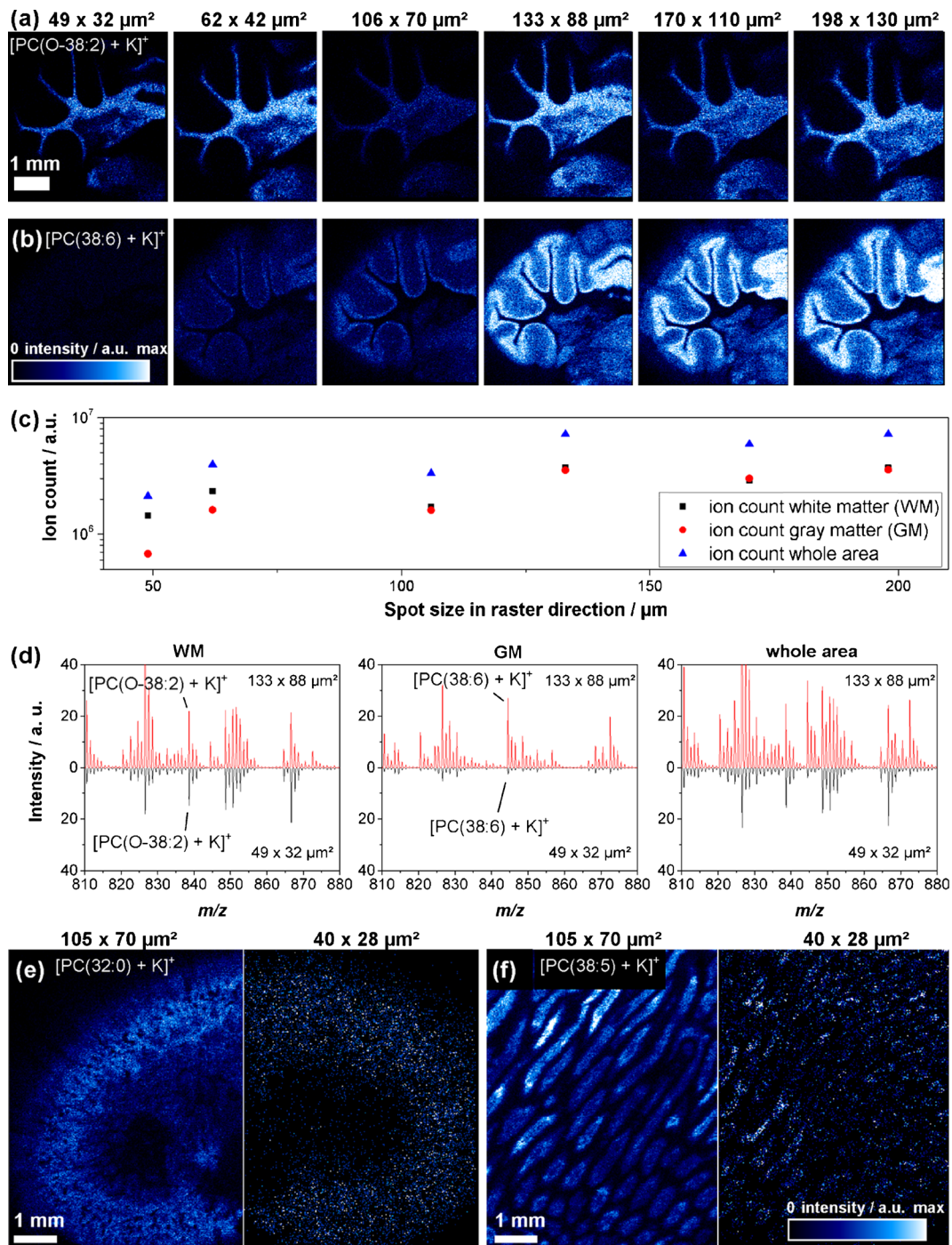


Figure 5. (a) Ion images of $[\text{PC}(\text{O-38:2}) + \text{K}]^+$ (m/z 838.62) obtained from six adjacent coronal mouse brain sections using different flat-top laser spot sizes; the plasmalogen is found solely in the WM. (b) Corresponding ion images of $[\text{PC}(38:6) + \text{K}]^+$ (m/z 844.52); this lipid species is most abundant in the GM; especially in the GL. (c) Total ion counts derived from WM and GM regions as well as from the whole tissue section as a function of laser spot size (the width in the raster direction is plotted); the m/z range from 650 to 1000 was evaluated. (d) Sum mass spectra of the three regions, acquired with focal spot sizes of $133 \times 88 \mu\text{m}^2$ (upper red trace) and $49 \times 32 \mu\text{m}^2$ (bottom gray trace); the m/z range from 810 to 880 is displayed. (e) MS images showing the distribution of $[\text{PC}(32:0) + \text{K}]^+$ at m/z 772.52 in longitudinal mouse kidney sections; data were acquired with flat-top spot sizes of $105 \times 70 \mu\text{m}^2$ (left) and $40 \times 28 \mu\text{m}^2$ (right). (f) Ion images of $[\text{PC}(38:5) + \text{K}]^+$ at m/z 846.55 obtained from longitudinal rat testis sections using the same two irradiation conditions as for mouse kidney. Mass spectra and MS images, respectively, were in all cases acquired in continuous raster mode and by applying a total of 30 laser shots per pixel at optimized laser fluence settings (cf. Figure 2 and Supplementary Table S1)

Tissue-Type Dependent Matrix Morphologies Investigated by SEM

To investigate if different matrix morphologies were produced on WM and GM, which could form the cause for the observed ion responses, we analyzed the mouse cerebellum sections (coated with sublimated/recrystallized DHB) by SEM. SEM images obtained after 3 and 8 min are plotted in Figure 6a–c and d–f, respectively. The images show that the matrix morphologies indeed vary with tissue type. After 3 min of sublimation, large variations of crystal morphology and coverage are apparent on the WM and GM (Figure 6a–c). While the thickness of the matrix layer is greatly increased at 8 min sublimation time, leading to a complete coverage of the whole sample, even here GM (lighter shade) and WM (darker shade of grey) can still be visually distinguished because of different matrix crystal morphology (Figure 6d). The figure shows the same brain structures as displayed in Figure 6a. Figure 6e and f show the morphologic differences in more detail.

These SEM images also visualize the laser ablation craters that were produced with a $106 \times 70 \mu\text{m}^2$ -wide flat-top laser beam (100 laser shots at 650 Jm^{-2} fluence were applied). Visually, they appear slightly smaller on the WM than the GM matter (Figure 6e).

Similar observations were recently made by Dowlatshahi Pour et al., who investigated matrix-enhanced secondary ion mass spectrometry (SIMS) [51]. These authors also used a

sublimation protocol for preparation of the matrix, but omitted the recrystallization step. Interestingly, different matrix-derived ion signals were detected from the WM and GM. For example, the radical molecular DHB matrix ion M^+ was almost solely detected from the WM areas. Although different volumes are analyzed with both methods—SIMS only analyzes the upper monolayers of the sample whereas the whole of the μm -thick matrix layers are sampled by MALDI—these results nevertheless corroborate distinct differences in matrix crystallization or analyte extraction depending on the brain region, as observed in the present MALDI experiments.

The Spot Size Effect

Our results showed that the fluence dependence of phospholipid ion generation as well as that for the TIC changed significantly for laser spot sizes below about $105 \times 70 \mu\text{m}^2$ (Figure 2e, f). This led to the use of elevated laser fluences to obtain optimal results at smaller spot sizes, in line with reported results [26–28]. However, apart from WM in brain sizably lower ion yields (ions per ablated material) were found with smaller spot sizes in oversampling experiments for complex MALDI-MSI measurements of lipids compared with laser spots above $105 \times 70 \mu\text{m}^2$.

We speculate that these distinct differences point to the transition between two material ejection regimes: at larger spots and concomitantly lower fluence a molecular quasi-thermal desorption is the predominant process of material ejection, whereas a more cluster-producing ablation process takes over at elevated fluences used for small spots [17, 19]. In contrast to studies conducted with less complex peptide samples, where the use of small spot sizes led to elevated ion yields [26–28], the detection of cationized phospholipids from tissue in the study at hand was favored using desorption as opposed to ablation conditions. In this respect, it might be expected that a spot size effect would not be limited to lipids but also occurs for MALDI-MSI of other important groups of analytes like peptides or metabolites. Additional investigations with suitable test systems and dedicated preparation protocols are needed to carefully investigate these considerations. The development and test of such systems was beyond the scope of the present study.

The magnitude of the observed spot size effect was largely dependent on differences in properties and conditions of the different tissue types. These could reflect differences in the morphology of the matrix coating and/or analyte extraction efficiencies during matrix application (Figure 6). The resulting differences in the matrix morphology could, in turn, lead to significant changes in the desorption/ionization mechanism, inherent to the MALDI process [17]. Certain matrix morphologies may be less susceptible to cluster formation at high fluences and, therefore, show less of an effect (e.g., the WM in cerebellum).

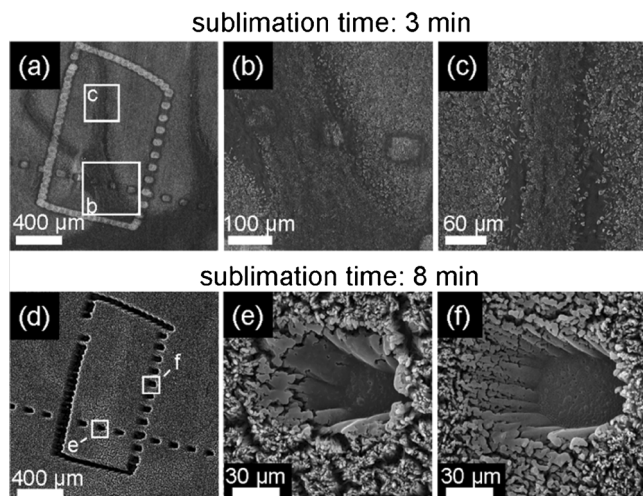


Figure 6. (a)–(c) SEM pictures of a coronal mouse brain section coated with a thin layer of DHB matrix obtained after 3 min of sublimation time; different magnifications are shown; 100 laser shots were applied in pixel-by-pixel mode and using a flat-top spot size of $106 \times 70 \mu\text{m}^2$. (d)–(f) SEM image of an adjacent mouse brain section after matrix sublimation for 8 min; the magnified views show laser ablation craters produced on (e) WM and (f) ML brain areas of the GM, respectively, using the same irradiation conditions. For better distinction of WM and GM in (d) contrast was slightly enhanced

Conclusions

We introduced a fundamental beam shaper for MALDI-MSI studies that enables rapid production of a square flat-top beam profile. Owing to the sharp flanks, this profile can provide advantageous properties for oversampling imaging experiments. Moreover, in contrast to excitation with a Gaussian laser beam, a homogenous energy deposition is readily achieved. Rapid switching between flat-top and Gaussian beams was possible by simply moving the FBS in and out of the laser beam path. Spot sizes in the range from 30 to 200 μm by width were produced with a telescope. Using the available multitude of different irradiation geometries, we analyzed the effects of flat-top versus Gaussian profiles, continuous raster mode versus pixel-by-pixel imaging, and, in particular, the spot size effect in MALDI-MSI oversampling experiments with a $20 \times 20 \mu\text{m}^2$ pixel area.

Surprisingly, with the exception of WM in cerebellum the spot size was found to have a large impact on the generation of lipid ion signals in oversampling experiments. We speculate that molecular desorption is the main mechanism of material ejection at larger spot sizes (and correspondingly lower fluences), whereas ablation of larger clusters is predominant at smaller spots (and higher fluence). This may lead to distinctively different and unfavorable ion yields for smaller spots also under non-oversampling conditions. To further complicate the matter, the extent of the spot size effect was found to strongly depend on the type of tissue (WM versus GM in cerebellum). SEM images revealed different matrix morphologies on these areas, which may be less susceptible to cluster formation at high fluences and, therefore, show less of an effect. Overall, our data indicate that sizably higher lipid ion yields were generally produced when oversampling experiments were performed with larger spot sizes and lower applied laser fluences (possibly the desorption regime) than with smaller laser spot sizes and elevated fluences (ablation regime). These advantages connected with the use of the larger laser spots, however, come with a certain loss in lateral resolution. Although speculative at this point, overall these findings could be suitable to trigger a new discussion about the fundamentals underlying the complex processes during the transition from an analyte inside a tissue sample to a mass spectrometric ion signal in the context of MALDI-MS imaging.

Analytically, the data indicate a high potential for MALDI-MSI using oversampling in continuous raster mode. Next to the obvious boost in acquisition speed, the laser spot size does not determine pixel size in oversampling experiments. Based on the obtained results, this allows for the optimization of laser spot size and fluence in order to achieve high analytical sensitivity for the desired analyte without compromising lateral resolution. The use of flat-top beam profiles in combination with high repetition rate lasers (e.g., in excess of 1 kHz) and dedicated sample stage designs could, in the future, decrease

the accessible pixel size to 10 μm and below and in turn increase lateral resolution for this rapidly developing technique.

Acknowledgments

Tissues were kindly provided by Jörg Haier (mouse brain and kidney) and Nicolas Schwab (rat testis). The authors thank Fabian Eiersbrock for help with preparation of tissue sections, Simeon Vens-Cappell for help with lipid assignments, and Andrej Shevchenko and Jens Höhdorf for support of the project. Financial support by the German Science Foundation (DFG) by grants SO 976/2-1 (to J.S.) and DR 416/9-1 (to K.D.), and the funds innovative medical research (grant I-SO 111518 to J.S.) and interdisciplinary center for clinical research (IZKF; grant Z03 to K.D.) of the Münster Medical School are gratefully acknowledged.

References

1. Norris, J.L., Caprioli, R.M.: Imaging mass spectrometry: a new tool for pathology in a molecular age. *Proteomics Clin. Appl.* **7**, 733–738 (2013)
2. Bhandari, D.R., Wang, Q., Friedt, W., Spengler, B., Gottwald, S., Römpf, A.: High resolution mass spectrometry imaging of plant tissues: towards a plant metabolite atlas. *Analyst* **140**, 7696–7709 (2015)
3. Zavalin, A., Todd, E.M., Rawhouser, P.D., Yang, J., Norris, J.L., Caprioli, R.M.: Direct imaging of single cells and tissue at sub-cellular spatial resolution using transmission geometry MALDI MS: single-cell imaging with transmission geometry. *J. Mass Spectrom.* **47**, 1473–1481 (2012)
4. Guenther, S., Römpf, A., Kummer, W., Spengler, B.: AP-MALDI imaging of neuropeptides in mouse pituitary gland with 5 μm spatial resolution and high mass accuracy. *Int. J. Mass Spectrom.* **305**, 228–237 (2011)
5. Römpf, A., Guenther, S., Schober, Y., Schulz, O., Takats, Z., Kummer, W., Spengler, B.: Histology by mass spectrometry: label-free tissue characterization obtained from high-accuracy bioanalytical imaging. *Angew. Chem. Int. Ed.* **49**, 3834–3838 (2010)
6. Korte, A.R., Yandau-Nelson, M.D., Nikolau, B.J., Lee, Y.J.: Subcellular-level resolution MALDI-MS imaging of maize leaf metabolites by MALDI-linear ion trap-Orbitrap mass spectrometer. *Anal. Bioanal. Chem.* **407**, 2301–2309 (2015)
7. Soltwisch, J., Kettling, H., Vens-Cappell, S., Wiegelmann, M., Müthing, J., Dreisewerd, K.: Mass spectrometry imaging with laser-induced postionization. *Science* **348**, 211–215 (2015)
8. Jurchen, J.C., Rubakhin, S.S., Sweedler, J.V.: MALDI-MS imaging of features smaller than the size of the laser beam. *J. Am. Soc. Mass Spectrom.* **16**, 1654–1659 (2005)
9. Garate, J., Fernández, R., Lage, S., Bestard-Escalas, J., Lopez, D.H., Reigada, R., Khorrani, S., Ginard, D., Reyes, J., Amengual, I., Barceló-Coblijn, G., Fernández, J.A.: Imaging mass spectrometry increased resolution using 2-mercaptobenzothiazole and 2,5-diaminonaphthalene matrices: application to lipid distribution in human colon. *Anal. Bioanal. Chem.* **407**, 4697–4708 (2015)
10. Snel, M.F., Fuller, M.: High-spatial resolution matrix-assisted laser desorption ionization imaging analysis of glucosylceramide in spleen sections from a mouse model of Gaucher disease. *Anal. Chem.* **82**, 3664–3670 (2010)
11. Spraggins, J.M., Caprioli, R.M.: High-speed MALDI-TOF imaging mass spectrometry: rapid ion image acquisition and considerations for next generation instrumentation. *J. Am. Soc. Mass Spectrom.* **22**, 1022–1031 (2011)
12. Trim, P.J., Djidja, M.-C., Atkinson, S.J., Oakes, K., Cole, L.M., Anderson, D.M.G., Hart, P.J., Francese, S., Clench, M.R.: Introduction of a 20 kHz Nd:YVO4 laser into a hybrid quadrupole time-of-flight mass spectrometer for MALDI-MS imaging. *Anal. Bioanal. Chem.* **397**, 3409–3419 (2010)
13. Simmons, D.A.: ABI technical note, improved MALDI-MS imaging performance using continuous laser rastering, document accessed on 2016/06/

- 28, available at: http://www.maldi-msi.org/download/TechNote_Raster_Imaging_QS.pdf. Accessed: (2008)
14. Karas, M., Bachmann, U., Bahr, U., Hillenkamp, F.: Matrix-assisted ultraviolet laser desorption of non-volatile compounds. *Int. J. Mass Spectrom. Ion Processes* **78**, 53–68 (1987)
 15. Wysocki, V.H., Resing, K.A., Zhang, Q., Cheng, G.: Mass spectrometry of peptides and proteins. *Methods* **35**, 211–222 (2005)
 16. Schiller, J., Süß, R., Fuchs, B., Müller, M., Zschörmig, O., Arnold, K.: MALDI-TOF MS in lipidomics. *Front. Biosci.* **12**, 2568–2579 (2007)
 17. Dreisewerd, K.: The desorption process in MALDI. *Chem. Rev.* **103**, 395–426 (2003)
 18. Knochenmuss, R.: Ion formation mechanisms in UV-MALDI. *Analyst* **131**, 966–986 (2006)
 19. Zhigilei, L.V., Leveugle, E., Garrison, B.J., Yingling, Y.G., Zeifman, M.I.: Computer simulations of laser ablation of molecular substrates. *Chem. Rev.* **103**, 321–348 (2003)
 20. Jaskolla, T.W., Karas, M.: Compelling evidence for lucky survivor and gas phase protonation: the unified MALDI analyte protonation mechanism. *J. Am. Soc. Mass Spectrom.* **22**, 976–988 (2011)
 21. Jaskolla, T.W., Lehmann, W.-D., Karas, M.: 4-Chloro- α -cyanocinnamic acid is an advanced, rationally designed MALDI matrix. *Proc. Natl. Acad. Sci. U. S. A.* **105**, 12200–12205 (2008)
 22. Knochenmuss, R., Dubois, F., Dale, M.J., Zenobi, R.: The matrix suppression effect and ionization mechanism in MALDI. *Rapid Commun. Mass Spectrom.* **10**, 871–877 (1996)
 23. Soltwisch, J., Jaskolla, T.W., Hillenkamp, F., Karas, M., Dreisewerd, K.: Ion yields in UV-MALDI mass spectrometry as a function of excitation laser wavelength and optical and physico-chemical properties of classical and halogen-substituted MALDI matrixes. *Anal. Chem.* **84**, 6567–6576 (2012)
 24. Wiegelmann, M., Soltwisch, J., Jaskolla, T.W., Dreisewerd, K.: Matching the laser wavelength to the absorption properties of matrices increases the ion yield in UV-MALDI mass spectrometry. *Anal. Bioanal. Chem.* **405**, 6925–6932 (2013)
 25. Soltwisch, J., Jaskolla, T.W., Dreisewerd, K.: Color matters—material ejection and ion yields in UV-MALDI mass spectrometry as a function of laser wavelength and laser fluence. *J. Am. Soc. Mass Spectrom.* **24**, 1477–1488 (2013)
 26. Dreisewerd, K., Schürenberg, M., Karas, M., Hillenkamp, F.: Influence of the laser intensity and spot size on the desorption of molecules and ions in matrix-assisted laser desorption/ionization with a uniform beam profile. *Int. J. Mass Spectrom. Ion Processes* **141**, 127–148 (1995)
 27. Qiao, H., Spicer, V., Ens, W.: The effect of laser profile, fluence, and spot size on sensitivity in orthogonal-injection matrix-assisted laser desorption/ionization time-of-flight mass spectrometry. *Rapid Commun. Mass Spectrom.* **22**, 2779–2790 (2008)
 28. Guenther, S., Koestler, M., Schulz, O., Spengler, B.: Laser spot size and laser power dependence of ion formation in high resolution MALDI imaging. *Int. J. Mass Spectrom.* **294**, 7–15 (2010)
 29. Steven, R.T., Race, A.M., Bunch, J.: Probing the relationship between detected ion intensity, laser fluence, and beam profile in thin film and tissue in MALDI MSI. *J. Am. Soc. Mass Spectrom.* (2016). doi:10.1007/s13361-016-1414-0
 30. Dreisewerd, K., Schürenberg, M., Karas, M., Hillenkamp, F.: Matrix-assisted laser desorption/ionization with nitrogen lasers of different pulse widths. *Int. J. Mass Spectrom. Ion Processes* **154**, 171–178 (1996)
 31. Knochenmuss, R., Vertes, A.: Time-delayed 2-pulse studies of MALDI matrix ionization mechanisms. *J. Phys. Chem. B* **104**, 5406–5410 (2000)
 32. Ingendoh, A., Karas, M., Hillenkamp, F., Giessmann, U.: Factors affecting the resolution in matrix-assisted laser desorption-ionization mass spectrometry. *Int. J. Mass Spectrom. Ion Processes* **131**, 345–354 (1994)
 33. Georgiou, S., Koubenakis, A.: Laser-induced material ejection from model molecular solids and liquids: mechanisms, implications, and applications. *Chem. Rev.* **103**, 349–394 (2003)
 34. Knochenmuss, R., Zhigilei, L.V.: Molecular dynamics model of ultraviolet matrix-assisted laser desorption/ionization including ionization processes. *J. Phys. Chem. B* **109**, 22947–22957 (2005)
 35. Knochenmuss, R., Zhigilei, L.V.: Molecular dynamics simulations of MALDI: laser fluence and pulse width dependence of plume characteristics and consequences for matrix and analyte ionization. *J. Mass Spectrom.* **45**, 333–346 (2010)
 36. Holle, A., Haase, A., Kayser, M., Höhndorf, J.: Optimizing UV laser focus profiles for improved MALDI performance. *J. Mass Spectrom.* **41**, 705–716 (2006)
 37. Römpp, A., Spengler, B.: Mass spectrometry imaging with high resolution in mass and space. *Histochem. Cell Biol.* **139**, 759–783 (2013)
 38. Dreisewerd, K.: Recent methodological advances in MALDI mass spectrometry. *Anal. Bioanal. Chem.* **406**, 2261–2278 (2014)
 39. Petković, M., Schiller, J., Müller, M., Benard, S., Reichl, S., Arnold, K., Arnold, J.: Detection of individual phospholipids in lipid mixtures by matrix-assisted laser desorption/ionization time-of-flight mass spectrometry: phosphatidylcholine prevents the detection of further species. *Anal. Biochem.* **289**, 202–216 (2001)
 40. Vens-Cappell, S., Kouzel, I.U., Kettling, H., Soltwisch, J., Bauwens, A., Porubsky, S., Müthing, J., Dreisewerd, K.: On-tissue phospholipase C digestion for enhanced MALDI-MS imaging of neutral glycosphingolipids. *Anal. Chem.* **88**, 5595–5599 (2016)
 41. Addie, R.D., Balluff, B., Bovée, J.V.M.G., Morreau, H., McDonnell, L.A.: Current state and future challenges of mass spectrometry imaging for clinical research. *Anal. Chem.* **87**, 6426–6433 (2015)
 42. Ellis, S., Bruinen, A.L., Heeren, R.M.A.: A critical evaluation of the current state-of-the-art in quantitative imaging mass spectrometry. *Anal. Bioanal. Chem.* **406**, 1275–1289 (2014)
 43. Yang, J., Caprioli, R.M.: Matrix sublimation/recrystallization for imaging proteins by mass spectrometry at high spatial resolution. *Anal. Chem.* **83**, 5728–5734 (2011)
 44. Kettling, H., Vens-Cappell, S., Soltwisch, J., Pirkl, A., Haier, J., Müthing, J., Dreisewerd, K.: MALDI mass spectrometry imaging of bioactive lipids in mouse brain with a Synapt G2-S mass spectrometer operated at elevated pressure: improving the analytical sensitivity and the lateral resolution to 10 μ m. *Anal. Chem.* **86**, 7798–7805 (2014)
 45. Yew, J.Y., Soltwisch, J., Pirkl, A., Dreisewerd, K.: Direct laser desorption ionization of endogenous and exogenous compounds from insect cuticles: practical and methodologic aspects. *J. Am. Soc. Mass Spectrom.* **22**, 1273–1284 (2011)
 46. Pirkl, A., Meier, M., Popkova, Y., Letzel, M., Schnapp, A., Schiller, J., Dreisewerd, K.: Analysis of free fatty acids by ultraviolet laser desorption ionization mass spectrometry using insect wings as hydrophobic sample substrates. *Anal. Chem.* **86**, 10763–10771 (2014)
 47. Wright, D.: Beamwidths of a diffracted laser using four proposed methods. *Opt. Quantum Electron.* **24**, 1129–1135 (1992)
 48. Wang, H.-Y.J., Liu, C.B., Wu, H.-W.: A simple desalting method for direct MALDI mass spectrometry profiling of tissue lipids. *J. Lipid Res.* **52**, 840–849 (2011)
 49. Gode, D., Volmer, D.A.: Lipid imaging by mass spectrometry – a review. *Analyst* **138**, 1289–1315 (2013)
 50. Fagerer, S.R., Römpp, A., Jefimovs, K., Brönnimann, R., Hayenga, G., Steinhoff, R.F., Krismer, J., Pabst, M., Ibáñez, A.J., Zenobi, R.: Resolution pattern for mass spectrometry imaging: resolution pattern for MSI. *Rapid Commun. Mass Spectrom.* **29**, 1019–1024 (2015)
 51. Dowlatshahi Pour, M., Malmberg, P., Ewing, A.: An investigation on the mechanism of sublimed DHB matrix on molecular ion yields in SIMS imaging of brain tissue. *Anal. Bioanal. Chem.* **408**, 3071–3081 (2016)